Kinetic Analysis of Free Radical Scavenging in Sonochemistry

Peng, Kewen; Tian, Shouceng; Zhang, Yiqun; Qu, Wanjun; Wang, Qianxi

DOI:
10.1016/j.cep.2023.109571

Kinetic Analysis of Free Radical Scavenging in Sonochemistry

Kewen Peng[1*], Shouceng Tian[2], Yiqun Zhang[2], Wanjun Qu[1], Qianxi Wang [3]

1. Guangdong Provincial Key Laboratory of Distributed Energy Systems
Dongguan University of Technology, Dongguan 523808, China

2. State Key Laboratory of Petroleum Resources and Prospecting
China University of Petroleum, Beijing 102249, China

3. School of Mathematics, University of Birmingham, Birmingham B15 2TT, United Kingdom

*Corresponding author: pengkw@dgut.edu.cn (K. Peng);

Abstract:

As an advanced oxidation process, high-power ultrasound produces free radicals in aqueous solution through acoustic cavitation. Whereas radical production inside the cavitation bubble is well understood, radical scavenging outside the bubble is still unexplored quantitatively. In this study, we modeled the behavior of radicals in the scavenging process by solving the diffusion-advection-reaction equations. Using terephthalate as the scavenger, the principal reaction pathways of hydroxyl radicals are identified and the scavenging efficiency is quantified. The analysis shows that among the various reactions competing for hydroxyl radicals, the scavenging by terephthalate is in disadvantage for the small mass diffusivity. It limits the replenishment of scavengers to the reaction zone and compromises radical trapping efficiency. A parametric study puts the maximum radical trapping efficiency below 30%. Our study elucidates the key factor limiting the utilization of ultrasound-induced radicals and paves the way for future efforts to maximize the sonochemical effects.

Keywords: Sonochemistry; Radical Scavenging; Cavitation; Bubble dynamics

1. Introduction

The physical-chemical effects associated with the irradiation of power ultrasound have found a variety of industrial applications such as materials synthesis[1-3], mixing and emulsification[4, 5], and degradation of hazardous substances [6, 7]. Ultrasonic treatment enjoys the advantages of being environmentally benign, versatile, and extremely highly efficient, among others [8].

As an advanced oxidation process, a salient attribute of the sonochemical effect is the generation of free radicals through acoustic cavitation [9, 10]. Under ultrasonic driving, the microbubbles undergo violent collapse, leading to the dissociation of water molecules into free radicals under extreme conditions within the cavity [11, 12]. When the radicals diffuse into the outside solutions, a cascade of redox reactions will be triggered and the chemical effects can be utilized [13, 14].

Mechanistically the potency of the sonochemical effects relies on not only the production of radicals inside the bubble, but also the scavenging of radicals by solutes surrounding the bubble as shown in Fig.1. While there are numerous studies devoted to the understanding of the first step [15-17], the latter is still uncharted territory. The knowledge gap hinders efforts from accurately evaluating the sonochemical yields to designing strategies to maximize radical utilization.

In this study, we aim to quantify the radical trapping efficiency by simulating the transport and reaction kinetics of the radicals in a typical scavenging process. The simulation is based on terephthalic acid (TA) dosimetry, a method widely used to measure the yield of hydroxyl radicals produced in sonochemistry. Correspondingly,

the scavenger is terephthalate. The TA dosimetry is chosen for the simulation to, firstly, take advantage of the nonvolatile property of terephthalate as a dissociated electrolyte. In this way, the scavenger is strictly confined in the solution and doesn't interfere with the production of radicals inside the bubble. Secondly, measurements of TA dosimetry in sonochemistry have long been troubled by the issue of underestimation [18-20]. With a closer observation of the simulated radical activities in the scavenger process, new insights can assist in better interpreting the underestimation.

The paper is structured as follows. In Section 2, the working principle of TA dosimetry to be simulated is introduced and the issue of underestimation of the measured radical yields in sonochemistry will be highlighted. In Section 3, the numerical model of radical production, diffusion, and reaction associated with acoustic cavitation is presented. The simulation results of the scavenging reaction are analyzed in Section. 4 and the implications on the radical measurement using TA dosimetry are discussed in Section 5. Finally, the main conclusions are summarized. To our best knowledge, this is the first quantitative investigation of radical scavenging in sonochemistry by complete numerical simulation. The reported findings can be useful for better grasping the key factors that influence the realization of the chemical potential of ultrasound.

2. Terephthalic acid dosimetry and the issue of underestimation

Currently, there are three widely used dosimetry methods to measure the yield of hydroxyl radicals produced in sonochemistry: Weissler [21], Fricke [22], and terephthalic acid (TA) [23]. From the perspective of the working principle, they can be

sorted into two categories. The TA dosimetry measures only the OH radicals that are intercepted by the scavenger (i.e. terephthalate anion) and is, therefore, a *direct* characterization approach. On the other side, Weissler and Fricke gauge the OH radical yield *indirectly*: the former infers the OH yield from the estimated amount of the recombination product H_2O_2, and the latter simultaneously measures $OH^{\bullet}$ and H_2O_2. The chemical reactions behind the three dosimetry methods are listed in Table 1.

The complete reaction mechanism of terephthalate dosimetry is based on the hydroxylation of terephthalate anion ($TER^{\bullet}$) by OH radicals [24]. The radicals are first added to the *ortho*-position of the aromatic ring of the terephthalate as shown in Fig. 2. Then, the intermediates, hydroxycyclohexadienyl radicals ($OH\text{-}TER^{\bullet}$), are oxidized to produce 2-hydroxyterephthalate ion (HTA). In our studied case, the oxidant is chosen as $IrCr_6^{2-}$ following Mark. et al. [20] and Iida et al.[18]. By measuring the concentration of the fluorescent HTA, the yield of OH radicals can be inferred. TA dosimetry has long been recommended for radical measurement due to its high sensitivity and easy operation [23].

In practice, however, rather than reporting data aligning with Weissler and Fricke dosimetry, the TA method in sonochemical application consistently underestimates the radical production. The anomaly has recently been highlighted through an analysis of previous measurement data [19]. Measured by the parameter of *G* value, defined as the number of $OH^{\bullet}$ produced per unit ultrasonic energy input, the TA-derived radical yield can be 30 times lower [18, 19]. On the other hand, Weissler and Fricke generally agree with each other in terms of the reported *G* value, suggesting their reliability [18, 19,

25].

To explore the cause of underestimation in TA dosimetry, Iida et al.[18] considered the influence of oxidants. They noticed that adding $IrCr_6^{2-}$ to the solution triples the *G* value compared with measurement without oxidants. Accordingly, they attributed the low measurement to the slow conversion from hydroxycyclohexadienyl radicals (OH-TER•) into 2-hydroxyterephthalate (See Step 2 in Fig. 2). However, this explanation is not convincing since the recalibrated radical yield is still lower than those that obtained from Weissler and Fricke dosimetry [18]. Besides, other TA tests using oxidants consistently reported the issue of underestimation [19, 20, 26]. The influence of the byproducts of hydroxylation reaction, such as 2, 5-dihydroxy terephthalic acid and 2-hydroxy terephthalic acid, has also been considered. However, it has been shown that their amounts are not large enough to account for the significant deviation [19]. In the present study, we examine the scavenging process directly to account for the underestimation and give a confidence interval for the estimated radical yields from TA dosimetry.

3. The numerical model

The analysis in our investigation is confined to a single spherical bubble oscillating in aqueous solutions under acoustic driving. The numerical model for simulating the radical behavior consists of two parts: one for radical production inside the bubble, and the other for radical dispersion in the outside liquid. The former has been presented in detail in our previous reports [27-31] and will therefore only be sketched briefly in Section 3.1. Then, the governing equations for radical dispersion in the solution are

introduced in Section 3.2.

3.1 Radical production inside the bubble

The model for radical production begins with the equation describing the radial oscillation of the bubble. In our simulation, the Gilmore equation is chosen [32],

$$\left(1-\frac{\dot{R}}{C}\right)R\ddot{R}+\frac{3}{2}\left(1-\frac{\dot{R}}{3C}\right)\dot{R}^2=\left(1+\frac{\dot{R}}{C}\right)H+\left(1-\frac{\dot{R}}{C}\right)\frac{R}{C}\dot{H}, \tag{1}$$

where R is the bubble radius, C the speed of sound in water and H the enthalpy evaluated at the bubble wall. The superposed dots denote derivatives with respect to time.

The pressure and temperature inside the bubble follow the van der Waals equation of state:

$$p_g=\frac{\mathcal{R}T_b}{\upsilon-b}-\frac{a}{\upsilon^2}, \tag{2}$$

with a and b denoting van der Waals constants, υ the molar volume of the gas mixture, and $\mathcal{R}$ the universal gas constant. The subscript 'g', 'l', and 'mix' thereafter refer to the gas, liquid, and gas mixture inside the bubble, respectively. The pressure p_g is related to the pressure in the liquid side at the bubble wall, p_b, as

$$p_g=p_b+\frac{2S}{R}+\frac{4\mu\dot{R}}{R}. \tag{3}$$

in which S and μ is the surface tension and viscosity of water, respectively.

The heat transfer inside the bubble is treated as a diffusion process through a thermal boundary layer:

$$\dot{Q}=4\pi R^2\kappa_{mix}\left(T_\infty-T_b\right)/\delta_g, \tag{4}$$

where κ_{mix} is the thermal conductivity of the gas mixture, T_∞ the ambient temperature, and δ_g the thickness of the thermal boundary layer. δ_g is estimated as a diffusion-

induced thermal penetration depth with an upper limit R/π [33]

$$\delta_g = \min\left(\left(\kappa_{mix}\Big/\left(\rho_{mix}c_{p,mix}\right)R\sqrt{\rho_l / p_b}\right)^{0.5}, R/\pi\right). \tag{5}$$

with the density ρ and heat capacity at constant pressure c_p.

Similarly, a thermal layer is assumed to be attached to the bubble in the liquid phase, through which heat conduction occurs. The thickness of this layer is estimated with [34]:

$$\delta_l = A_T \times \min\left\{\left(\frac{\kappa_l}{\rho_l c_{pl}}\frac{R}{\sqrt{p/\rho_l}}\right)^{1/2}, \frac{4\pi R^2\kappa_l}{L|\dot{n}_v|}\right\} \tag{6}$$

where L is the heat of vaporization and $|\dot{n}_v|$ the net flux of vapor due to vaporization and condensation. A_T is the scaling constant, A_T =1.3 [34]. The above relation considers two time scales Δt to estimate heat transfer: one for the bubble motion $\Delta t = R(p/\rho_l)^{-1/2}$, and another for the phase change $\Delta t = \rho_l 4\pi R^2 \delta_l c_{pl}/L|\dot{n}_v|$. Then the thickness is calculated as $\delta = \sqrt{D_l \Delta t} = \sqrt{k_l/\rho_l c_{pl}\Delta t}$, where D_l is the thermal diffusivity.

The temperature T_i at the bubble interface is determined by enforcing the continuity of heat flux:

$$4\pi R^2\kappa_l \left.\frac{\partial T_l}{\partial r}\right|_{r=R} - 4\pi R^2\kappa_g \left.\frac{\partial T_g}{\partial r}\right|_{r=R} = L\dot{n}_v \tag{7}$$

For the mass transfer across the bubble interface, we only consider water vapor and free radicals while disregarding those with low or moderate solubility such as H_2 and O_2. This simplification is based on the short time duration (~60 T_a, T_a =1/f) covered by the present simulation compared with that needed for noticeable mass transfer for these species (~ fR^2/D_m ~ 3900T_a, where D_m is the mass diffusivity). The evaporation

and condensation of water are modeled by the Hertz–Knudsen–Langmuir formula [35-37]:

$$\dot{n}_{\mathrm{H_2O}} = 4\pi R^2 \frac{\alpha_M \left(p_{sat} - p_v \right)}{\sqrt{2\pi M_{\mathrm{H_2O}} \mathcal{R} T_b}}. \tag{8}$$

This equation gives the rate of change of water molecules as a function of the saturated vapor pressure p_{sat} and the partial pressure of vapor inside the bubble p_v. The molecular weight M_{H2O}=18 g/mol and the accommodation coefficient α_M =0.4.

The interfacial flux of free radicals across the bubble wall (in the unit of number per surface area per time) is estimated with [38, 39]

$$\Gamma_i = \Theta c_{i,1} \sqrt{\frac{k_B T_b}{2\pi M_i}}. \tag{9}$$

where $c_{i,1}$ is the concentration of species i inside the bubble and Θ is the uptake coefficient, Θ =0.001. In this study, we consider a bubble initially filled with water vapor and argon only. Their amounts at the equilibrium state are determined according to the saturated vapor pressure p_{sat} and the partial pressure p_g - p_{sat}, respectively [15, 40].

When the bubble collapses violently, the water vapor is dissociated into free radicals under rising temperature and pressure. The intracavity chemistry therein is modeled with the GRI-Mech 3.0 mechanism. The species, reaction rate coefficients, and thermodynamics for this mechanism can be accessed through the database [41]. The incorporation of chemistry simulation into the dynamic model is accomplished through the open-source platform Cantera [42].

The above equations enclose the model of radical production. Further details in

terms of the numerical implementation can be found elsewhere [27-31]. From this model, the real-time bubble radius *R*, bubble wall velocity $\dot{R}$, and radical flux Γ_i can be obtained. They will be used as input parameters for the simulation of radical dispersion in the outside liquid, which will be introduced below.

3.2 Radical dispersion in the outside liquid

For the chemical reactions occurring in the aqueous phase surrounding the argon bubble, we consider 11 species of relevance as listed in Table 2. Among them, the radicals, $H^{\bullet}$, $OH^{\bullet}$, O, and $HO_2^{\bullet}$, are originated from chemical reactions inside the bubble and dissolve into the solution at the interface. The molecular species, H_2O_2, H_2, and O_2, are the products of the reactions among the radicals in the liquid phase. Finally, the species, $TER^{\bullet}$, $IrCr_6^{2-}$, OH-$TER^{\bullet}$, and HTA, are the reactants or products involved in the scavenging reactions related to TA dosimetry. The diffusivity of each species is also given in the table. They are referenced from Ref. [43] except for the last 4 species, for which the common value for ions, 1.0×10^{-5} cm^2/s, is adopted due to a lack of relevant data. Their precise diffusivity may differ slightly, but the influence on the simulation results can be safely disregarded. In Table. 3, the reactions occurring in the aqueous phase together with the rate coefficients are summarized [24, 43, 44].

The dispersion of radicals in the bulk liquid is a coupled nonlinear advection-diffusion-reaction process. The concentration c_i for the species *i* is a function of time *t* and radial position *r*, which is dictated by [27, 28]

$$\frac{\partial c_i}{\partial t}+\dot{R}\left(\frac{R}{r}\right)^2\frac{\partial c_i}{\partial r}=\frac{D_i}{r^2}\frac{\partial}{\partial r}\left(r^2\frac{\partial c_i}{\partial r}\right)+\sum_j \alpha_{i,j}\gamma_j\,, \qquad r\in[R,\infty]. \tag{10}$$

where D_i denotes the diffusivity of the species. Note that this equation is similar to the

equation describing heat transfer in the liquid [45] except for the addition of the last term, which represents the concentration variation due to chemical reactions. In the above equation, γ_j denotes the reaction rate and $\alpha_{i,j}$ the stoichiometric weight of species i in the reaction j. As stated above, the bubble radius R and velocity $\dot{R}$ in the equation comes from the dynamic simulation. The radicals are supplied from the bubble with the interfacial flux calculated by Eq. 7. At the far field, their concentrations are considered to have reached asymptotic value. Therefore, the advection-diffusion-reaction equation (Eq.8) is subject to the following boundary conditions:

$$D_i \frac{\partial c_i}{\partial r} = \Gamma_i, \qquad r = R \ , \tag{11}$$

$$\frac{\partial c_i}{\partial r} = 0 , \qquad r \to \infty . \tag{12}$$

For the species involved in the scavenging reactions (TER$^{\bullet}$, $IrCr_6^{2-}$, OH-TER$^{\bullet}$, HTA), zero flux condition is imposed at the bubble wall. At the far field, constant concentration $c=c_0$ is assumed since the dimension of the reaction zone is small compared with that of the bulk solution.

As will be shown later, the release of radicals from the bubble interface to the surrounding solutions is intense and transient. A steep concentration gradient is formed within a thin boundary layer. Once dissolved in the solution, they are quickly consumed by chemical reactions. As a result, the concentration profile of radicals evolves rapidly. Extremely fine resolution on both the spatial and temporal dimensions is required to capture the concentration field. In the simulation, we approximate the concentration field by Chebyshev polynomials and enforce the equation on Gauss-Lobatto collocation

points to ensure accuracy. Temporally, we vary the number of polynomials instantly based on the evolution of the concentration profile to advance the solution efficiently. The details of the numerical implementation are given in Appendix. A and the validation of the whole model is discussed in Appendix. B.

When the bubble collapses violently, the liquid layer surrounding the bubble will be heated dramatically. Strictly speaking, the modeling of chemical reactions should account for the thermal effects by solving the partial differential equation governing the heat transfer in the liquid phase. However, the exact temperature dependence of the elementary reactions listed in Table 3 is unknown. Therefore, we ignored the temperature rise in the liquid during the simulation and assumed constant rate coefficients for the chemical reactions. Following the same reasoning, the concentration of the molecular species H_2 and O_2 in the liquid phase is capped at their saturation value at ambient room temperature, i.e., 0.80 and 0.28 mol/m^3, respectively. The possible implications of the thermal effects are discussed in Appendix. C.

4. Results

4.1 Simulation design

The simulation discussed in the following sections is based on the TA test of Mark et al.[20], where the initial concentration of terephthalate and the oxidant $IrCr_6^{2-}$ in the solution is 2 and 0.2 mol/m^3, respectively. The solution is saturated with argon and sonicated by ultrasound with frequency f=321 kHz and pressure amplitude p_a=3 bar. The equilibrium radius of the simulated argon bubble R_e= 3.5 μm.

When evaluating the radical trapping efficiency, it is important to note the small

mass diffusivity of the reactants and the role it may play in the scavenging reaction. To comprehend this issue, we emphasize that the diffusivity of both the free radicals and terephthalate is on the order of 10^{-5} cm^2/s, while the rate coefficients of the involved chemical reactions are up to 10^{10} M^{-1}/s as can be seen from Table.2 and 3, respectively. The contrast in the values of these parameters implies that the radicals can't travel much distance in the solution before being depleted quickly in the chemical reactions [27]. As will be shown later, the reaction zone is restricted within a thin boundary layer adjacent to the bubble interface with a thickness of ~1 μm. This means for the scavenging reaction, the reactant $TER^{\bullet}$ must be replenished from the outer parts of the solution to the boundary layer once it is consumed. Owing to the small diffusivity, the replenishment may not be timely, which will diminish or disrupt the scavenging reactions and consequently result in a lower efficiency of radical trapping. Similar restricting effects imposed by small mass diffusivity are seen in rectified diffusion for an oscillating bubble, where millions of acoustic cycles are required for observable bubble growth [46].

To examine the influence of mass diffusivity on the radical trapping efficiency in TA dosimetry, two cases are simulated and compared. In Case A, the diffusivity of terephthalate and $IrCr_6^{2-}$ is the normal value, 1.0×10^{-5} cm^2/s, as listed in Table 2. In Case B, the diffusivity is assumed to be infinite, indicating the reactants are replenished instantly once consumed. This translates into unaltered concentration, i.e., 2 and 0.2 mol/m^3, for these two reactants throughout the dynamic process. All the other parameters are the same for the two cases.

The assumption made in Case B may seem counterintuitive at first glance. However, it bears a certain resemblance to the realistic environment that a bubble faces in the solution. Firstly, rather than being levitated at a fixed location as assumed in the simulation, the bubble in actual sonochemical reactors makes coupled volumetric oscillations and translations. Along the traveling process, the bubble surface continuously meets new, and presumably pristine, solutions where the concentration of terephthalate and $IrCr_6^{2-}$ are the initial values. Secondly, an oscillatory bubble in a real ultrasonic field is accompanied by microstreaming around its surface. This would result in enhanced mixing and may bring more solutes to the boundary layer. Thirdly, due to the extremely low solubility, the terephthalic acid tends to accumulate in the boundary layer. While these factors are ignored in the simulation, they all assist in replenishing the reactants more efficiently for the scavenging reactions. In a real scenario, the actual concentration of terephthalate and $IrCr_6^{2-}$ probably falls somewhere between values dictated by Case A and B. It is noted that Sonntag et al. [47] made a similar assumption of a constant concentration of terephthalic acid when discussing the suppression on the formation of hydrogen peroxide by radical scavengers.

4.2 Radical release and penetration

In this section, we show a typical picture of radical release from the oscillating bubble and its penetration in the surrounding aqueous phase. The illustrative example is based on Case A. The results are extracted from the dynamic simulation after 30 acoustic cycles to exclude the initial transient effects.

Figure 3 (a) presents the variation of the bubble radius spanning 5 acoustic cycles.

The bubble is seen to oscillate stably at the prescribed acoustic driving, with alternating expansion and compression. The radius in the former stage increases to about $6.75R_0$ before shrinking to only $0.17R_0$ in the collapse. As a result of compressional heating, the temperature of the gases in the collapsing bubble rises sharply and peaks at about 6826 K. The extreme conditions therein trigger the thermal dissociation of water molecules and produce various free radicals, including $H^{\bullet}$, $OH^{\bullet}$, O, and $HO_2^{\bullet}$. As we demonstrated earlier [28, 29], the concentrations of these radicals can reach up to hundreds of moles per cubic meter within the compressed bubble. Driven by the concentration gradient, they diffuse into the surrounding liquid from the bubble surface. The interfacial flux for the three main radicals, $H^{\bullet}$, $OH^{\bullet}$, and O, estimated by Eq.7 is displayed in Fig. 3(b). It shows that the release of the radicals is transient but intense, similar to the nature of bubble collapse.

Fig. 3(c)-(e) present the evolving concentration field of the three main radicals in the solution adjacent to the bubble. As the radical concentration range spans over two orders of magnitude but clusters heavily around the low end, concentrations larger than 0.5 mol/m^3 are not differentiated but colored red in the figure to avoid blurring of the penetration picture. Fig. 3(f)-(h) display a close-up of the radical penetration around the time of the third bubble collapse for each radical. The figures indicate that after entering the aqueous phase, the radicals diffuse briefly in the solution before being consumed by the chemical reactions. The penetration depth for the main radicals is on the order of micrometer and their existence in the liquid lasts hundreds of microseconds, in agreement with our previous studies [27, 28]. In addition, the existence of this layer is

seen to be intermittent and concurrent with the bubble collapse.

For individual radical particles, it has been reported that the lifetime of OH radicals in the liquid is about 20 ns and the diffusion length is around 13 nm [48]. This estimation is based on the initial concentration of OH radicals and the rate coefficient of the reactions consuming the radicals. However, as the chemical scheme listed in Table.3 indicates, additional OH radicals may be produced in the liquid phase by reactions such as R5 and R12-15. This feature complicates the effort of lifetime estimation by only considering the consuming reactions. Also, the Eulerian approach used in the present study doesn't allow us to track individual particles. As a result, a direct comparison between the penetration behavior of radicals reported in the literature and that from our study is not possible. For the O radicals, it has been proposed that some radicals may be in an excited state, $O(^1D)$, when being produced in the bubble [49]. In this case, the reaction $O(^1D)+ H_2O \rightarrow H_2O_2$ dominates the dynamics of O radicals in the liquid due to the large rate of this reaction $k=1.8\times10^{10}$ $M^{-1}s^{-1}$ [50]. We conducted another simulation by including this reaction (not shown here) and found the penetration depth of O radicals at several nanometers. As the proportion of excited radicals is unknown, the exact penetration depth of O radicals remains to be explored.

At the bulk period between radical releases, the solution near the bubble is void of radicals. The intermittent existence suggests that the radicals are consumed rather quickly in an acoustic cycle once they are released into the liquid. This is caused by the dense particle population in the boundary layer combined with the high reactivity of free radicals. As can be seen from the chemical scheme listed in Table. 3, the primary

reactions consuming OH radicals are recombination $OH^{\bullet}_{(aq)}+OH^{\bullet}_{(aq)}\rightarrow H_2O_{2(aq)}$, reaction with H radicals $H^{\bullet}_{(aq)}+ OH^{\bullet}_{(aq)}\rightarrow H_2O_{(aq)}$, and the reaction with terephthalate $TER^{\bullet}_{(aq)} + OH^{\bullet}_{(aq)}\rightarrow OH\text{-}TER^{\bullet}_{(aq)}$. Note the rate of the last reaction, 3.3×10^{9} $M^{-1}s^{-1}$, is on the same level as the other two reactions (3.6×10^{9} and 7.0×10^{9}, respectively).

4.3 Competition between radical recombination and scavenging reaction

We now focus on the competition for OH radicals between radical recombination ($OH^{\bullet}_{(aq)}+OH^{\bullet}_{(aq)}\rightarrow H_2O_{2(aq)}$) and the reaction with terephthalate ($TER^{\bullet}_{(aq)} + OH^{\bullet}_{(aq)}\rightarrow OH\text{-}TER^{\bullet}_{(aq)}$, $OH\text{-}TER^{\bullet}_{(aq)} + IrCr^{2-}_{6}(aq)\rightarrow HTA_{(aq)}$) by analyzing the indicator product H_2O_2 and HTA. The third reaction, $H^{\bullet}_{(aq)}+ OH^{\bullet}_{(aq)}\rightarrow H_2O_{(aq)}$, is not monitored but its influence can be assumed as similar to that of the recombination reaction owing to the identical radical concentration level and reaction rate. For H_2O_2 formed in the solution, it may also come from the reaction $HO_{2(aq)}^{\bullet}+HO_{2(aq)}^{\bullet}\rightarrow H_2O_{2(aq)}+ O_{2(aq)}$. However, our simulation shows that there is only a trace amount of HO_2 produced from the argon bubble. Therefore, H_2O_2 can be reliably regarded as the indicator product of the recombination reaction.

Figure 4 compares the evolution of the concentration field of HTA during the initial 60 acoustic cycles in Cases A and B. It is observed that the formation of HTA is intermittent corresponding to the cyclic release of OH radicals. Unlike OH radicals, however, the generated HTA is not consumed by other reactions but accumulated in the solution. This leads to an ever-expanding concentration profile towards the outer solution. A comparison of Fig. 4(a) and (b) immediately illustrates the higher efficiency in the production of HTA in Case B. The difference becomes progressively pronounced

after 20 cycles. The propagation front of HTA in Case B is observed to quickly reach the radial position of 10 μm. In contrast, the accumulation of HTA in Case A is much slower. At the end of the investigated period, the maximum concentration is only 1.7 mol/m^3, while this value is 5.5 mol/m^3 in Case B.

As the scavenging reaction is strengthened under an abundant supply of terephthalate, the recombination reaction is suppressed as displayed in the comparison of Fig. 5(a) and (b). The production of H_2O_2 is observed to be much more intensive in Case A than in Case B. To quantify the production of HTA and H_2O_2, the particle number N, $N=\int_R^\infty 4\pi r^2 c dr$, of these two species existing in the solution is calculated and plotted against the time in Fig.6. It suggests the change in the relative advantage of the recombination and scavenging reaction in Case A and B.

It is noteworthy that even under infinite mass diffusivity (Case B), H_2O_2 is still massively produced as displayed in Fig. 5(b), showing an active recombination reaction occurring in the boundary layer. Together with the radical reaction $H^{\bullet}_{(aq)} + OH^{\bullet}_{(aq)} \rightarrow H_2O_{(aq)}$, it consumes a large proportion of OH radicals released from the bubble. At the end of the simulation ($t=60T_a$), 49% of the total OH radicals released in the solution recombine or react with other radicals, meaning only half of the radicals are trapped by the terephthalate. This feature indicates an inherent deficiency of direct radical measurement methods such as TA dosimetry: they can trap only a part of radicals even in most preferential conditions. Underestimation in the radical yield is thus unavoidable with these methods.

4.4 The effect mechanism of diffusion

In normal circumstances (Case A), the underestimation is further worsened with only 35% of the radicals trapped by terephthalate within the simulated 60 acoustical cycles. To account for the decreased radical trapping efficiency in Case A, we turn our intention back to the scavenging reaction $TER^{\bullet}_{(aq)} + OH^{\bullet}_{(aq)} \rightarrow OH\text{-}TER^{\bullet}_{(aq)}$ and investigate the supply of the reactants to the reaction zone, i.e., the boundary layer. Fig.7 (a) and (b) present the distribution of terephthalate anion $TER^{\bullet}$ and $OH^{\bullet}$ in this case within the first 60 acoustic cycles. The results show that while the supply of OH radicals is stable among different cycles, that of $TER^{\bullet}$ varies significantly. During the initial 24 acoustic cycles, the concentration front of $TER^{\bullet}$ in Fig. 7(a) retreats from the bubble wall continuously, indicating the depletion of this reactant in the boundary layer due to the scavenging reaction with OH radicals. As a result, the amount of radicals trapped by the scavenger $TER^{\bullet}$ in an acoustic cycle decreases, leaving more radicals to recombine or react with other radicals.

As the solution near the bubble is increasingly void of $TER^{\bullet}$, the adverse concentration gradient strengthens and propels $TER^{\bullet}$ back to the boundary layer through diffusion. This is reflected in the 25th cycle in Fig. 7(a) when the concentration front of $TER^{\bullet}$ moves inward and reaches the near field again. Consequently, the intensity of the scavenging reaction is restored with more reactants in the boundary layer now. After that, the depletion of $TER^{\bullet}$ occurs again and the retreat of the concentration front reappears. Fig. 7(a) shows that the retreat and advance of the concentration front repeat about every 5 acoustic cycles. The fraction of OH radicals, η, trapped by terephthalate

in a single acoustic cycle in the latter stage is shown in Fig.8. The influence of varying reactant supply on the scavenging reaction can be seen by the fluctuation of η.

4.5 Radical trapping efficiency

Figure 9 displays the radical trapping efficiency by the scavengers η at different acoustic pressure amplitudes with the constant frequency of f=100 kHz. It shows that the η varies significantly among different acoustic cycles. Overall, the trapping efficiency is lower than 30% and trends downwards with time. The average η during the investigated period is summarized in Table 4. A positive relationship between the radical trapping efficiency and the acoustic intensity is observed. However, this association should be treated with caution due to the transient nature of η and the limited number of acoustic periods that our simulation covers. As Fig.9 indicates, the trapping efficiency is expected to be lower as the bubble oscillation and scavenging reactions proceed.

5. Discussion

In principle, the measurement accuracy of TA dosimetry is determined by the efficiency of OH radicals being trapped by the terephthalate anion ($TER^{\bullet}$) in the solution. As simple as it seems, it represents the most obscure part of sonochemistry at large. As illustrated in Fig. 1, the radicals escaping from the bubble and entering the bulk liquid undergo complex physical and chemical transitions. On the physical side, diffusion under concentration gradients propels the radicals to penetrate deep into the liquid. On the chemical side, due to the high reactivity, the radicals go through intense reactions along the dispersion process, including radical recombination ($OH^{\bullet}+OH^{\bullet}\rightarrow$

H_2O_2), the reaction with other radicals (e.g. $OH^{\bullet}+H^{\bullet}\rightarrow H_2O$), and scavenging reaction ($OH^{\bullet}+TER^{\bullet}\rightarrow HTA$). These reactions compete for OH radicals released from the cavitation bubble. Therefore, it is conceivable that, firstly, underestimation in TA dosimetry is inevitable. Secondly, the accuracy of TA dosimetry is determined by the exact proportion of radicals that are trapped by scavenging reactions.

The simulation result confirms the above hypothesis and further highlights the inherent deficiency of direct radical measurement approaches such as TA dosimetry: owing to the highly reactive nature, a large proportion of OH radicals are inevitably consumed through recombination and other radical reactions. This issue is compounded by the tendency that these reactions are strengthened nonlinearly when more radicals are released into the boundary layer. In this regard, direct methods like TA cannot accurately quantify the produced OH radicals. Indirect methods such as Weissler and Fricke dosimetry seem more suitable for such analysis.

Secondly, we demonstrated that insufficient replenishment of terephthalate due to small diffusivity further weakens radical trapping efficiency. Our simulation shows that less than 30% of the radicals can be trapped by terephthalate. Previous test [19] reported that the overall concentration of terephthalate in the solution doesn't decrease significantly after 30 min of sonication, indicating the amount of consumed terephthalate in a TA test is very small. Combined with our findings in this study, the low yield of OH radicals measured from TA dosimetry is reconfirmed and explained.

In actuality, some favorable factors can alleviate the constraint on radical trapping efficiency in TA dosimetry. For example, bubble translation, microstreaming, and

hydrophobicity are beneficial in bringing more terephthalate particles into the boundary layer. Advanced numerical methods are required to investigate their influences.

6. Conclusion

In this paper, we numerically simulated the radical scavenging process surrounding a cavitation bubble in TA dosimetry. The employed model covers bubble dynamics, intracavity chemistry, and radical dispersion in the solution. To deal with the steep mass concentration gradient near the bubble interface, the Chebyshev spectral collocation method combined with variable polynomial numbers is employed. The role of mass diffusion in the underestimation of hydroxyl radicals in TA dosimetry is examined by assuming two cases: an infinite and a normal diffusivity of terephthalate.

The in-depth observation on the radical transport and conversion reveals rich patterns of radical activities surrounding the collapsing cavitation bubble. Firstly, a high-resolution picture of radical release and penetration in the liquid phase is presented. Then, by showing the robust production of hydrogen peroxide even in the case of infinite terephthalate diffusivity, the occurrence of strong radical recombination is confirmed and the deficiency of TA dosimetry in characterizing radical yields is therefore demonstrated. The derived radical trapping efficiency provides a reference for the use of terephthalic acid dosimetry in sonochemistry

By comparing the formation of 2-hydroxyterephthalate, the indicator product of the scavenging reaction, in the two cases, the key factor limiting effective radical scavenging is pinpointed. We showed that the small diffusivity of terephthalate causes the slow replenishment of the reactants to the reaction zone and weakens the radical

trapping efficiency. In this regard, in order to promote the utilization of radicals in sonochemistry, more efforts should be focused on developing techniques to enhance diffusion and mixing in the near field of the bubble.

Acknowledgment

This work was supported by the National Key Research and Development Program (No. 2019YFA0708300), Guangdong Basic and Applied Basic Research Foundation (No. 2019A1515110755 and 2020A1515110665), and Guangdong Provincial University Innovation Team Project (No. 2023KCXTD038). We thank the anonymous referees for the careful reviews and useful suggestions, which improve the manuscript greatly.

Appendix A

In this section, we detail the solution strategy in solving the partial differential equation (PDE) (Eq. 8) governing the dispersion of chemical species in solution. The PDE describes two processes with distinct time scales: the slow mass advection-diffusion, and the ultrafast chemical reactions. Their dynamic features are indicated by the small value of diffusivity in Table. 2 and the large reaction rate coefficient in Table. 3. Correspondingly, the stiffness of the equations for the two processes is vastly different. To freely choose an integration strategy pertinent to the individual equation, the whole PDE is split and solved separately using an approach proposed by Qu and Garfinkel [51]. At each time step Δt, the following advection-diffusion equation is integrated first with the Matlab solver ode45 over the half-step length Δt /2:

$$\frac{\partial c_i}{\partial t}+\dot{R}\left(\frac{R}{r}\right)^2\frac{\partial c_i}{\partial r}=\frac{D_i}{r^2}\frac{\partial}{\partial r}\left(r^2\frac{\partial c_i}{\partial r}\right),\qquad r\in[R,\infty]. \tag{A1}$$

Next, the reaction equation is integrated by the Matlab stiff solver ode15s over the full step Δt using the results from the first step as the initial condition:

$$\frac{\partial c_i}{\partial t}=\sum_j \alpha_{i,j}\gamma_j\ . \tag{A2}$$

Finally, the advection equation is integrated again using Matlab solver ode45 over the remaining Δt /2, with the updated concentration from the reaction step.

A tricky issue in solving Eq.A1 is the moving boundary at the bubble surface (r=R). To deal with the equation in a fixed framework, a transformation technique [52] is adopted. It first introduces a radial variable y=r/R(t) and converts the coordinate into ξ,

$$\xi=\frac{L}{L+y-1}\ ,\ \xi\in(0,\ 1], \tag{A3}$$

where L represents the scale of diffusion distance,

$$L=l\left(\frac{D_i}{\omega R_e^2}\right)^{0.5}\ , \tag{A4}$$

where ω is the angular frequency of ultrasound and l =20 is the scaling constant following Kamath et al. [40]. After transformation, the advection equation becomes

$$\frac{\partial c}{\partial t}=\left(\frac{\zeta}{L}\right)^2\frac{D}{R^2}\zeta^2\frac{\partial^2 c}{\partial\zeta^2}+\left\{\left(\frac{\zeta}{L}\right)^2\frac{D}{R^2}2\zeta-\frac{\zeta^2}{L}\left[\frac{2D}{yR^2}+\frac{\dot{R}}{R}\left(y-\frac{1}{y^2}\right)\right]\right\}\frac{\partial c}{\partial\zeta}. \tag{A5}$$

For brevity, subscript i denoting the species will be omitted hereinafter. Now, our focus is to solve Eq. A5. From previous studies [27, 28], it is known that the concentration gradient is steep across the boundary layer adhering to the bubble surface. To yield a concentration field with high accuracy, the Chebyshev spectral collocation method is employed in solving Eq. A5. Considering the zero gradients at the far field

boundary (ξ=0) for the radicals and molecular species, we follow Storey and Szeri [53] and use only even Chebyshev polynomials T_{2k} with the highest order of $2N$ to approximate the concentration profile:

$$c = \sum_{k=0}^{N} a_k T_{2k}(\zeta) \quad , \tag{A6}$$

where T_{2k}=cos($k\theta$), θ=arccos ζ, and a_k is the coefficient to be determined. By enforcing the equation at the Gauss-Lobatto collocation points

$$\zeta = \cos(j\pi/2N), \quad j = 0, 1, ..., N, \tag{A7}$$

we obtain N+1 equations

$$\sum_{k=0}^{N} T_{2k} \frac{\partial a_k}{\partial t} = \sum_{k=0}^{N} \chi_k a_k, \tag{A8}$$

with

$$\chi_k = \left(\frac{\zeta_k}{L}\right)^2 \frac{D}{R^2} \zeta_k{}^2 \frac{\partial^2 T_{2k}}{\partial \zeta^2} + \left\{ \left(\frac{\zeta_k}{L}\right)^2 \frac{D}{R^2} 2\zeta_k - \frac{\zeta_k^2}{L} \left[\frac{2D}{y_k R^2} + \frac{\dot{R}}{R}\left(y_k - \frac{1}{y_k^2} \right) \right] \right\} \frac{\partial T_{2k}}{\partial \zeta}. \tag{A9}$$

At the bubble wall (ξ=1), the boundary condition of interfacial flux (Eq. 9) translates into

$$D \left.\frac{\partial c}{\partial r}\right|_{r=R} = D \left.\frac{\partial c}{\partial \zeta}\frac{\partial \zeta}{\partial r}\right|_{r=R} = -\frac{D}{LR} \left.\frac{\partial c}{\partial \zeta}\right|_{\zeta=1} = \Gamma, \tag{A10}$$

which provides a constraint to the system of equations:

$$\sum_{k=0}^{N} a_k \left.\frac{\partial T_{2k}}{\partial \zeta}\right|_{\zeta=1} = -\frac{LR}{D}\Gamma. \tag{A11}$$

For the 4 species (TER$^{\bullet}$, IrCr2- 6, OH-TER$^{\bullet}$, HTA) involved in the scavenging reactions, the odd Chebyshev polynomials in addition to T_0=1 are used due to the constant boundary condition at infinite.

Even with the advantage of being able to achieve high accuracy with relatively

low computational demand, we found the spectrum method still needs at most over 100 polynomials in some steps to yield a refined concentration profile. This is attributed to, again, the steep concentration gradient within the boundary layer in our case. The difficulty in the simulation is further compounded by the computational burden that Eq. A5 is required to be solved 11 times at each step for the 11 species listed in Table 3.

Luckily, an important feature of radical dispersion allows varying the number of polynomials dynamically in the calculation and thus lessens the requirement on computation resources significantly. Following the cyclic expansion and compression of the oscillating bubble, the concentration profile steepens only around the point of bubble collapse as a result of intense radical release into the surrounding solution. During the bulk of the period, however, the profile is relatively smooth and can be readily resolved. We take this advantage by monitoring the ratio of the first to the last coefficient of the approximating Chebyshev polynomials. When this ratio exceeds 1.0×10^{-4} suggesting a steepening concentration profile, two additional polynomials are added to the sequence in the next step. On the other hand, when the ratio falls below 1.0×10^{-5} indicating the tendency of profile flattening, the two trailing polynomials are subtracted from the series. With this strategy, the number N of polynomials stays around 50 most of the time and the computation can be conducted efficiently.

Appendix B

The validation of the simulated results is challenging due to the transient nature (~μs) and small scale (~μm) of the investigated problem. To our best knowledge, there are no reported tests with such a fine resolution that can depict the radical concentration

field around a single cavitation bubble. To circumvent the difficulty, an indirect approach is employed.

The complete numerical model consists of two parts: one for radical production (Eq. 1-6), and the other for dispersion (Eq. 8-10). The latter is free of adjustable parameters and should yield reliable results by using the highly accurate spectral method. Then, the accuracy of the whole simulation depends on the first submodel. In our previous studies, we checked the validity of this submodel on two aspects: dynamically [29], the ability to accurately reproduce the evolution of bubble radius in multiple collapse-rebound cycles using the test data of Sato et al. [54]; Chemically[27], the model predicts the calibrated number of produced OH radicals with an error smaller than an order of magnitude compared with experimental results of Didenko & Suslick [55]. Still, we admit the comparison on the chemical aspect represents a rough agreement at best. However, as the focus of the present study is centered on the behavior of radicals *after* they diffuse into the solution, which, again, is described by the second submodel without adjustable parameters, we are content with the performance of the numerical model.

Appendix C

During the simulation of chemical reactions in the liquid phase, the thermal effect is ignored. However, it has long been recognized that a high-temperature liquid layer (sketched in Fig.A1) is formed during the bubble collapse, which serves as an important site for chemical reactions [56]. The influence of this thermal layer is discussed in this section.

The activities of radicals include radical formation inside the bubble, and consumption in the surrounding liquid phase, one after the other. The former is realized under extreme conditions in the collapsing bubble, while the latter is caused by various chemical reactions such as recombination between radicals and scavenging by solutes in the liquid. Contrary to the first-sight impression that radical activities in the heated liquid layer belong to the second category, we argue that for the better part of bubble collapse, radicals are still produced in this layer, rather than being consumed.

We prove our argument as follows. In Fig.A2 (a) and (b), the temperature and pressure in the thermal layer during a typical bubble collapse are shown. They are calculated using the approximated relations Eq.6 and 7 introduced in the numerical model section. The peak temperature of 1200 K qualitatively agrees with the extent of temperature rise reported by Suslick et al. [56]. More importantly, Fig.A2 (a) and (b) collectively demonstrate that the temperature and pressure in the thermal boundary layer can easily pass the critical point of water (T=647.15 K and p=22.1 MPa).

For water in the *supercritical* state, there is no distinction between liquid and gas. On the other hand, radical reactions are still happening. These reactions are traditionally treated as those occurring in combustion [57-59], where the radicals are generated in high-temperature conditions. Note that at the end of the collapse, the water vapor inside the bubble is also in the supercritical state. In this regard, the thermal layer can be categorized as the inner part of the bubble and the chemistry therein can be considered to have been accounted for when the radical production inside the bubble is simulated.

Now we consider the period in Fig.A2 (a) when the liquid temperature is lower

than the critical temperature (647.15 K) but higher than the ambient temperature (293 K). At enhanced temperatures, both the radical reactions and scavenging reactions will accelerate. To estimate the increase in radical reaction rate, we refer to the relations compiled by Matsui et al. [60] shown in Table. A1. Based on these relations, the rate coefficients for the three representative reactions at T=293 K and 647 K reactions are obtained and listed in the last two columns. The results indicate an average increase of about two orders of magnitude for the rate coefficients. Note that the reaction of utmost concern, $OH^{\cdot}_{(aq)} + OH^{\cdot}_{(aq)} \rightarrow H_2O_{2(aq)}$, seems to be temperature-independent from the relation.

For the radical scavenging reaction $TER^{\cdot}_{(aq)} + OH^{\cdot}_{(aq)} \rightarrow OH\text{-}TER^{\cdot}_{(aq)}$, Charbouillot et al. [61] reported the dependence of OH-TER yield on the temperature in the range of 278 K to 303 K as $Y_{\text{OH-TER}}=(0.0059\pm0.0011)T-(1.50\pm0.31)$. Extrapolating this relation to the temperature range discussed here, an increase of tenfold in the reaction rate is estimated.

Apart from these reactions, the temperature dependence of rate coefficients for other reactions listed in Table 3 is not known, which impedes a complete evaluation of the thermal influence on the radical scavenging efficiency. Despite this knowledge shortfall, the apparent large variation in the rate coefficients caused by temperature rise should not be a major concern. Judging from the standards of errors in reaction rate, a discrepancy of two orders of magnitude is not rare in chemical modeling. Such a discussion on the uncertainty of reaction simulation was recently conducted by Kalmár et al. [62]. They compared three reaction mechanisms widely used in sonochemistry

and highlighted the difference in the reaction rate of several orders of magnitude.

At last, we discuss the pyrolysis of terephthalic acid (TA) in the liquid thermal layer. According to the test of Kimyonok and Ulutürk [63], TA begins to decompose into benzoic acid at 863.15 K and undergoes further conversion to smaller compounds. It is noted that the threshold temperature of TA pyrolysis is higher than the critical temperature of water as indicated in Fig.A2 (a). In Fig.A2(c), the thickness of the liquid thermal layer is plotted as a function of time. It shows that when the water is in supercritical state and the TA pyrolysis occurs, the boundary layer is extremely thin, i.e., about 9 nm as can be seen in Fig.A2(c). Compared with the penetration depth of over 500 nm for hydroxyl radicals as displayed in Fig.A2(d), the influence range of TA pyrolysis is negligible. Therefore, they are not considered in the simulation.

References:

[1] J. Balachandramohan, R. Singh, T. Sivasankar, S. Manickam, Sonochemical synthesis of highly efficient Ag3PO4-Guar gum nanocomposite with photo-oxidation property under visible light irradiation, Chemical Engineering and Processing - Process Intensification, 168 (2021) 108549.

[2] S.E. Karekar, D.V. Pinjari, Sonochemical synthesis and characterization of molybdenum sulphide nanoparticles: Effect of calcination temperature, Chemical Engineering and Processing - Process Intensification, 120 (2017) 268-275.

[3] S. Barcikowski, A. Plech, K.S. Suslick, A. Vogel, Materials synthesis in a bubble, MRS Bulletin, 44 (2019) 382-391.

[4] L. Patil, P.R. Gogate, Large scale emulsification of turmeric oil in skimmed milk using different cavitational reactors: A comparative analysis, Chemical Engineering and Processing - Process Intensification, 126 (2018) 90-99.

[5] A.S. Peshkovsky, S.L. Peshkovsky, S. Bystryak, Scalable high-power ultrasonic technology for the production of translucent nanoemulsions, Chemical Engineering and Processing: Process Intensification, 69 (2013) 77-82.

[6] O. Moumeni, O. Hamdaoui, C. Pétrier, Sonochemical degradation of malachite green in water, Chemical Engineering and Processing: Process Intensification, 62 (2012) 47-53.

[7] D. Panda, V. Sethu, S. Manickam, Kinetics and mechanism of low-frequency ultrasound driven elimination of trace level aqueous perfluorooctanesulfonic acid and perfluorooctanoic acid, Chemical Engineering and Processing - Process Intensification, 142 (2019) 107542.

[8] R.J. Wood, J. Lee, M.J. Bussemaker, A parametric review of sonochemistry: control and augmentation

of sonochemical activity in aqueous solutions, Ultrasonics sonochemistry, 38 (2017) 351-370.
[9] S. Sochard, A.M. Wilhelm, H. Delmas, Gas-vapour bubble dynamics and homogeneous sonochemistry, Chemical Engineering Science, 53 (1998) 239-254.
[10] A. Dehane, S. Merouani, O. Hamdaoui, Effect of carbon tetrachloride (CCl4) sonochemistry on the size of active bubbles for the production of reactive oxygen and chlorine species in acoustic cavitation field, Chemical Engineering Journal, 426 (2021) 130251.
[11] G.L. Lee, M.C. Law, Numerical modelling of single-bubble acoustic cavitation in water at saturation temperature, Chemical Engineering Journal, 430 (2022) 133051.
[12] J. Ma, G.L. Chahine, C.-T. Hsiao, Spherical bubble dynamics in a bubbly medium using an Euler–Lagrange model, Chemical Engineering Science, 128 (2015) 64-81.
[13] S.K. Bhangu, M. Ashokkumar, Theory of Sonochemistry, in: J.C. Colmenares, G. Chatel (Eds.) Sonochemistry: From Basic Principles to Innovative Applications, Springer International Publishing, Cham, 2017, pp. 1-28.
[14] K. Fattahi, E. Robert, D.C. Boffito, Numerical and experimental investigation of the cavitation field in horn-type sonochemical reactors, Chemical Engineering and Processing - Process Intensification, 182 (2022) 109186.
[15] C. Kalmár, K. Klapcsik, F. Hegedűs, Relationship between the radial dynamics and the chemical production of a harmonically driven spherical bubble, Ultrasonics Sonochemistry, 64 (2020) 104989.
[16] A. Dehane, S. Merouani, A. Chibani, O. Hamdaoui, M. Ashokkumar, Influence of processing conditions on hydrogen Sonoproduction from methanol sono-conversion: A numerical investigation with a validated model, Chemical Engineering and Processing - Process Intensification, 179 (2022) 109080.
[17] M. Hamida, A. Dehane, S. Merouani, O. Hamdaoui, M. Ashokkumar, The role of reactive chlorine species and hydroxyl radical in the ultrafast removal of Safranin O from wastewater by CCl4/ultrasound sono-process, Chemical Engineering and Processing - Process Intensification, 178 (2022) 109014.
[18] Y. Iida, K. Yasui, T. Tuziuti, M. Sivakumar, Sonochemistry and its dosimetry, Microchemical Journal, 80 (2005) 159-164.
[19] D.B. Rajamma, S. Anandan, N.S.M. Yusof, B.G. Pollet, M. Ashokkumar, Sonochemical dosimetry: A comparative study of Weissler, Fricke and terephthalic acid methods, Ultrasonics Sonochemistry, 72 (2021) 105413.
[20] G. Mark, A. Tauber, R. Laupert, H.-P. Schuchmann, D. Schulz, A. Mues, C. von Sonntag, OH-radical formation by ultrasound in aqueous solution – Part II: Terephthalate and Fricke dosimetry and the influence of various conditions on the sonolytic yield, Ultrasonics Sonochemistry, 5 (1998) 41-52.
[21] T. Kimura, T. Sakamoto, J.-M. Leveque, H. Sohmiya, M. Fujita, S. Ikeda, T. Ando, Standardization of ultrasonic power for sonochemical reaction, Ultrasonics Sonochemistry, 3 (1996) S157-S161.
[22] A.K. Jana, S.N. Chatterjee, Estimation of hydroxyl free radicals produced by ultrasound in Fricke solution used as a chemical dosimeter, Ultrasonics Sonochemistry, 2 (1995) S87-S91.
[23] T.J. Mason, J.P. Lorimer, D.M. Bates, Y. Zhao, Dosimetry in sonochemistry: the use of aqueous terephthalate ion as a fluorescence monitor, Ultrasonics Sonochemistry, 1 (1994) S91-S95.
[24] X. Fang, G. Mark, C. von Sonntag, OH radical formation by ultrasound in aqueous solutions Part I: the chemistry underlying the terephthalate dosimeter, Ultrasonics Sonochemistry, 3 (1996) 57-63.
[25] S. Koda, T. Kimura, T. Kondo, H. Mitome, A standard method to calibrate sonochemical efficiency of an individual reaction system, Ultrasonics Sonochemistry, 10 (2003) 149-156.
[26] I. Hua, M.R. Hoffmann, Optimization of Ultrasonic Irradiation as an Advanced Oxidation Technology,

Environmental Science & Technology, 31 (1997) 2237-2243.
[27] K. Peng, S. Tian, Y. Zhang, Q. He, Q. Wang, Penetration of hydroxyl radicals in the aqueous phase surrounding a cavitation bubble, Ultrasonics Sonochemistry, 91 (2022) 106235.
[28] K. Peng, F.G.F. Qin, R. Jiang, W. Qu, Q. Wang, Production and dispersion of free radicals from transient cavitation Bubbles: An integrated numerical scheme and applications, Ultrasonics Sonochemistry, 88 (2022) 106067.
[29] K. Peng, F.G.F. Qin, R. Jiang, W. Qu, Q. Wang, Reactive species created in the collapse of laser-induced cavitation bubbles: Generation mechanism and sensitivity analysis, Journal of Applied Physics, 131 (2022) 043101.
[30] K. Peng, F.G.F. Qin, S. Tian, Y. Zhang, An inverse method to fast-track the calculation of phase diagrams for sonoluminescing bubbles, Ultrasonics Sonochemistry, 73 (2021) 105534.
[31] K. Peng, F.G.F. Qin, R. Jiang, S. Kang, Interpreting the influence of liquid temperature on cavitation collapse intensity through bubble dynamic analysis, Ultrasonics Sonochemistry, 69 (2020) 105253.
[32] F. Gilmore, The growth or collapse of a spherical buble in a viscous compressible liquid, California Institute of Technology, Hydrodynamics Laboratory, Pasadena, California, USA, Report No. 26-4, (1952).
[33] R. Toegel, B. Gompf, R. Pecha, D. Lohse, Does water vapor prevent upscaling sonoluminescence?, Physical review letters, 85 (2000) 3165.
[34] W. Kreider, L.A. Crum, M.R. Bailey, O.A. Sapozhnikov, A reduced-order, single-bubble cavitation model with applications to therapeutic ultrasound, The Journal of the Acoustical Society of America, 130 (2011) 3511-3530.
[35] S. Fujikawa, T. Akamatsu, Effects of the non-equilibrium condensation of vapour on the pressure wave produced by the collapse of a bubble in a liquid, Journal of Fluid Mechanics, 97 (1980) 481-512.
[36] I. Akhatov, O. Lindau, A. Topolnikov, R. Mettin, N. Vakhitova, W. Lauterborn, Collapse and rebound of a laser-induced cavitation bubble, Physics of Fluids, 13 (2001) 2805-2819.
[37] X. Zhong, J. Eshraghi, P. Vlachos, S. Dabiri, A.M. Ardekani, A model for a laser-induced cavitation bubble, International Journal of Multiphase Flow, 132 (2020) 103433.
[38] B.D. Storey, A.J. Szeri, Water vapour, sonoluminescence and sonochemistry, Proceedings of the Royal Society of London. Series A: Mathematical, Physical and Engineering Sciences, 456 (2000) 1685-1709.
[39] K. Yasui, T. Tuziuti, M. Sivakumar, Y. Iida, Theoretical study of single-bubble sonochemistry, The Journal of chemical physics, 122 (2005) 224706.
[40] A. Dehane, S. Merouani, Impact of dissolved rare gases (Ar, Xe and He) on single-bubble sonochemistry in the presence of carbon tetrachloride, Chemical Papers, 76 (2022) 3011-3030.
[41] G.P. Smith, D.M. Golden, M. Frenklach, N.W. Moriarty, B. Eiteneer, M. Goldenberg, C.T. Bowman, R.K. Hanson, S. Song, W.C. Gardiner, J. Lissianski, Vitali V., Z. Qin, Gri-mech 3.0., see: http://combustion.berkeley.edu/gri-mech/.
[42] D.G. Goodwin, R.L. Speth, H.K. Moffat, B.W. Weber, Cantera: An object-oriented software toolkit for chemical kinetics, thermodynamics, and transport processes, Doi: 10.5281/zenodo.4527812, see: https://www.cantera.org.
[43] W. Tian, M.J. Kushner, Atmospheric pressure dielectric barrier discharges interacting with liquid covered tissue, Journal of Physics D: Applied Physics, 47 (2014) 165201.
[44] J. Jiang, Z. Tan, C. Shan, J. Pan, G. Pan, Y. Liu, X. Chen, X. Wang, A new study on the penetration of reactive species in their mass transfer processes in water by increasing the electron energy in plasmas, Physics of Plasmas, 23 (2016) 103503.

[45] F. Hegedűs, C. Hős, L. Kullmann, Influence of heat transfer on the dynamic response of a spherical gas/vapour bubble, International Journal of Heat and Fluid Flow, 31 (2010) 1040-1049.
[46] W.R. Smith, Q. Wang, A tractable mathematical model for rectified diffusion, Journal of Fluid Mechanics, 951 (2022) A12.
[47] C. von Sonntag, G. Mark, A. Tauber, H.-P. Schuchmann, OH radical formation and dosimetry in the sonolysis of aqueous solutions, Advances in Sonochemistry, 5 (1999) 109-145.
[48] K. Yasui, Acoustic Cavitation and Bubble Dynamics, Springer Cham, 2018, pp. 26.
[49] K. Yasui, Production of O Radicals from Cavitation Bubbles under Ultrasound, Molecules, 27 (2022).
[50] D. Biedenkapp, L.G. Hartshorn, E.J. Bair, The O(1D) + H2O reaction, Chemical Physics Letters, 5 (1970) 379-381.
[51] Z. Qu, A. Garfinkel, An advanced algorithm for solving partial differential equation in cardiac conduction, IEEE Transactions on Biomedical Engineering, 46 (1999) 1166-1168.
[52] V. Kamath, A. Prosperetti, F.N. Egolfopoulos, A theoretical study of sonoluminescence, The Journal of the Acoustical Society of America, 94 (1993) 248-260.
[53] B.D. Storey, A.J. Szeri, Mixture segregation within sonoluminescence bubbles, Journal of Fluid Mechanics, 396 (1999) 203-221.
[54] T. Sato, M. Tinguely, M. Oizumi, M. Farhat, Evidence for hydrogen generation in laser-or spark-induced cavitation bubbles, Applied Physics Letters, 102 (2013) 074105.
[55] Y.T. Didenko, K.S. Suslick, The energy efficiency of formation of photons, radicals and ions during single-bubble cavitation, Nature, 418 (2002) 394-397.
[56] K.S. Suslick, The site of sonochemical reactions, IEEE transactions on ultrasonics, ferroelectrics, and frequency control, 33 (1986) 143-147.
[57] E.E. Brock, P.E. Savage, Detailed chemical kinetics model for supercritical water oxidation of C1 compounds and H2, AIChE Journal, 41 (1995) 1874-1888.
[58] B.D. Phenix, J.L. Dinaro, M.A. Tatang, J.W. Tester, J.B. Howard, G.J. McRae, Incorporation of parametric uncertainty into complex kinetic mechanisms: Application to hydrogen oxidation in supercritical water, Combustion and Flame, 112 (1998) 132-146.
[59] J.M. Ploeger, P.A. Bielenberg, J.L. Dinaro-Blanchard, R.P. Lachance, J.D. Taylor, W.H. Green, J.W. Tester, Modeling oxidation and hydrolysis reactions in supercritical water—free radical elementary reaction networks and their applications, Combustion Science and Technology, 178 (2006) 363-398.
[60] Y. Matsui, N. Takeuchi, K. Sasaki, R. Hayashi, K. Yasuoka, Experimental and theoretical study of acetic-acid decomposition by a pulsed dielectric-barrier plasma in a gas–liquid two-phase flow, Plasma Sources Science and Technology, 20 (2011) 034015.
[61] T. Charbouillot, M. Brigante, G. Mailhot, P.R. Maddigapu, C. Minero, D. Vione, Performance and selectivity of the terephthalic acid probe for OH as a function of temperature, pH and composition of atmospherically relevant aqueous media, Journal of Photochemistry and Photobiology A: Chemistry, 222 (2011) 70-76.
[62] C. Kalmár, T. Turányi, I.G. Zsély, M. Papp, F. Hegedűs, The importance of chemical mechanisms in sonochemical modelling, Ultrasonics Sonochemistry, 83 (2022) 105925.
[63] A.B. Elmas Kimyonok, M. Ulutürk, Determination of the Thermal Decomposition Products of Terephthalic Acid by Using Curie-Point Pyrolyzer, Journal of Energetic Materials, 34 (2016) 113-122.

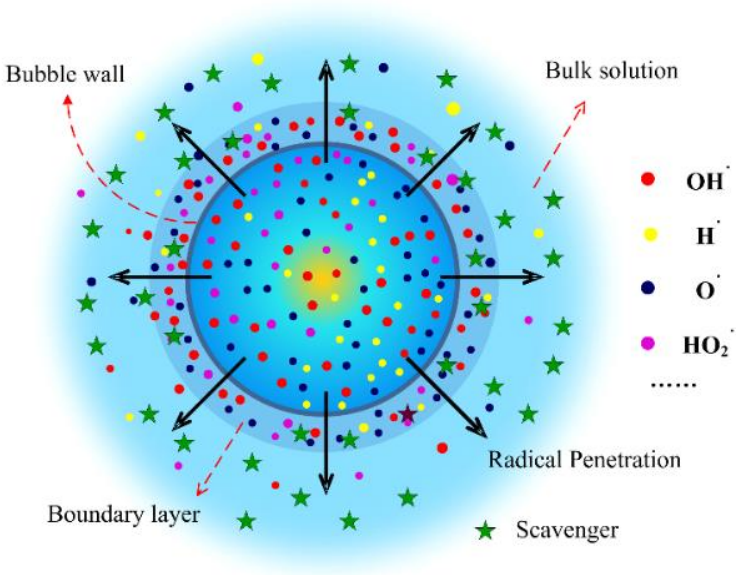

Fig. 1 Schematic showing the radical production inside the cavitation bubble and scavenging in the outside solution.

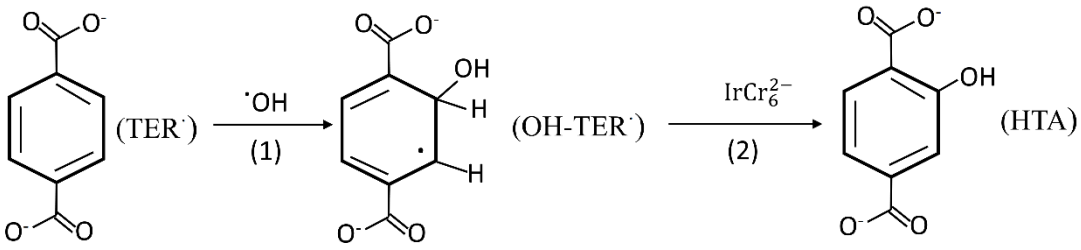

Fig. 2 Reaction pathway in terephthalate dosimetry

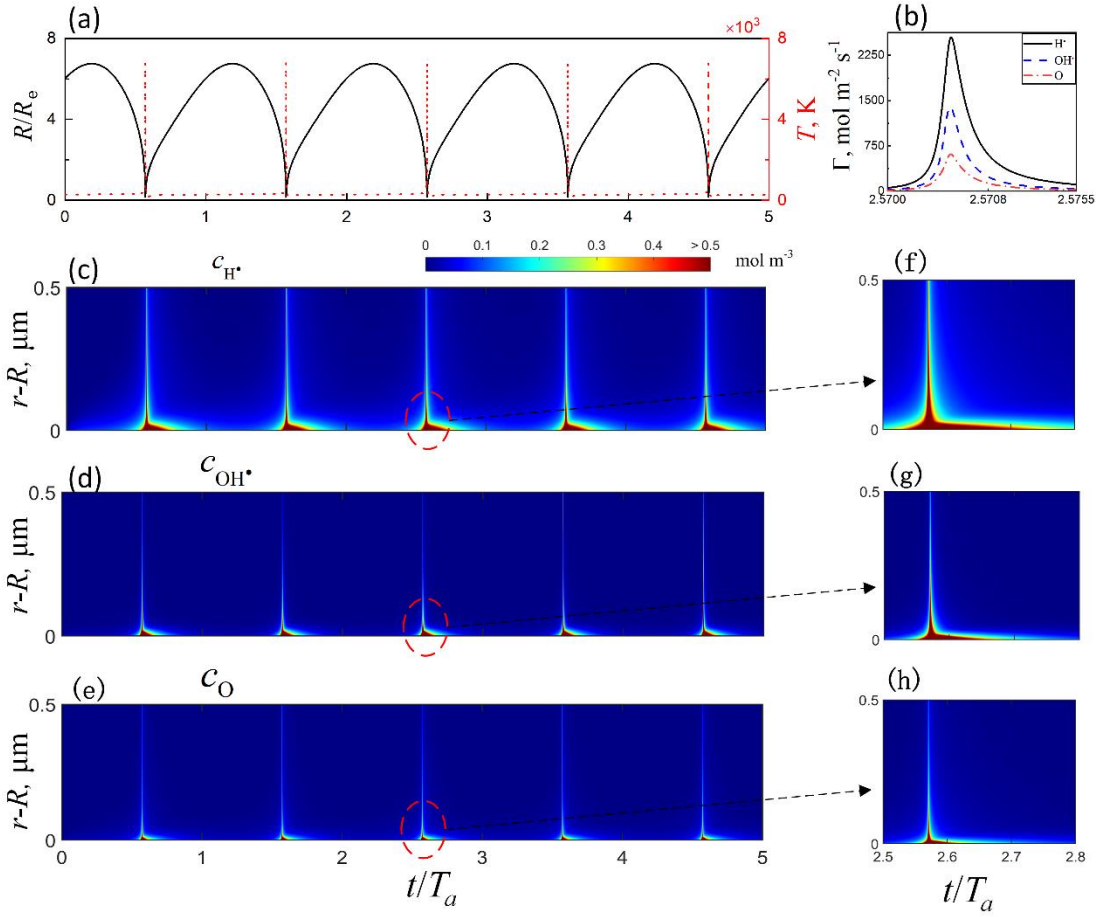

Fig. 3 The release and penetration of free radicals in the liquid phase. (a) The bubble dynamics displayed in the form of radius evolution over 5 acoustic cycles; (b) The interfacial flux of H•, OH•, and O around the point of the third bubble collapse; (c-e) The contour of the concentration field showing the penetration of radicals. It is displayed in the space occupied by the liquid adjacent to the bubble with $r>R$; (f-h) A close-up of radical penetration around the point of the third bubble collapse. For illustrative purposes, radical concentration larger than 0.5 mol/m^3 is not differentiated but colored red. The max concentration for H•, OH•, and O is 436.8, 417.5, and 168.4 mol/m^3, respectively. The simulation is based on Case A, where the parameters are: p_a=3 bar, f= 321 kHz, R_e=3.5 μm, and T_∞=293 K. The abscissa in the figures is the time t scaled by the acoustical period T_a, T_a =1/f.

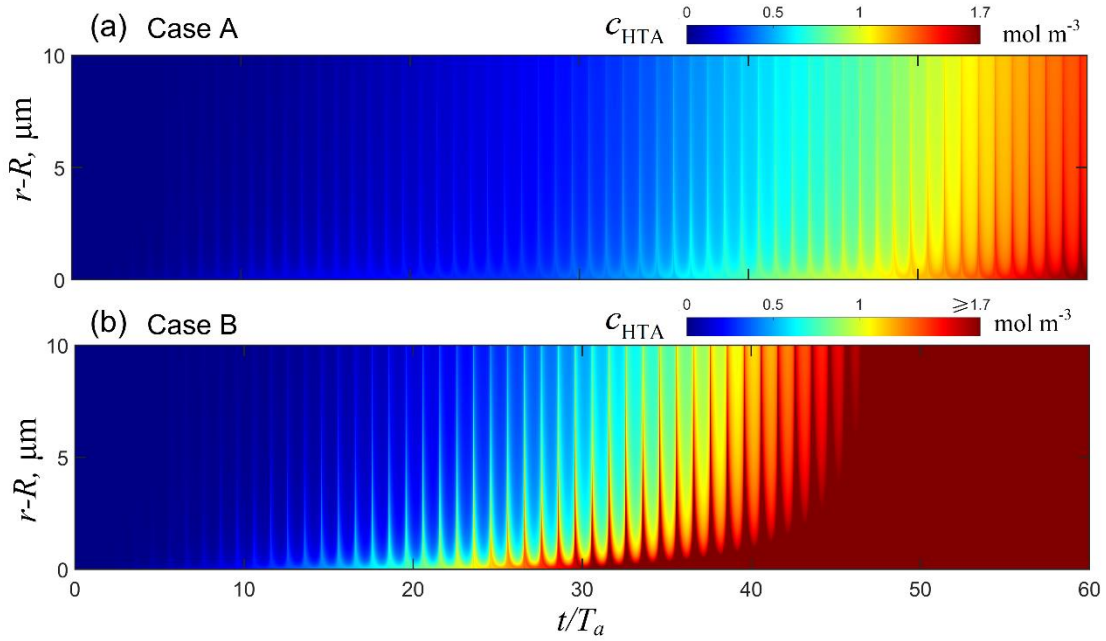

Fig. 4 The formation of HTA within a period of 60 acoustic cycles in Case A and B. The maximum concentration is 1.7 mol/m^3 in Case A and 5.5 mol/m^3 in Case B. For comparison, the same color bar is applied in (a) and (b).

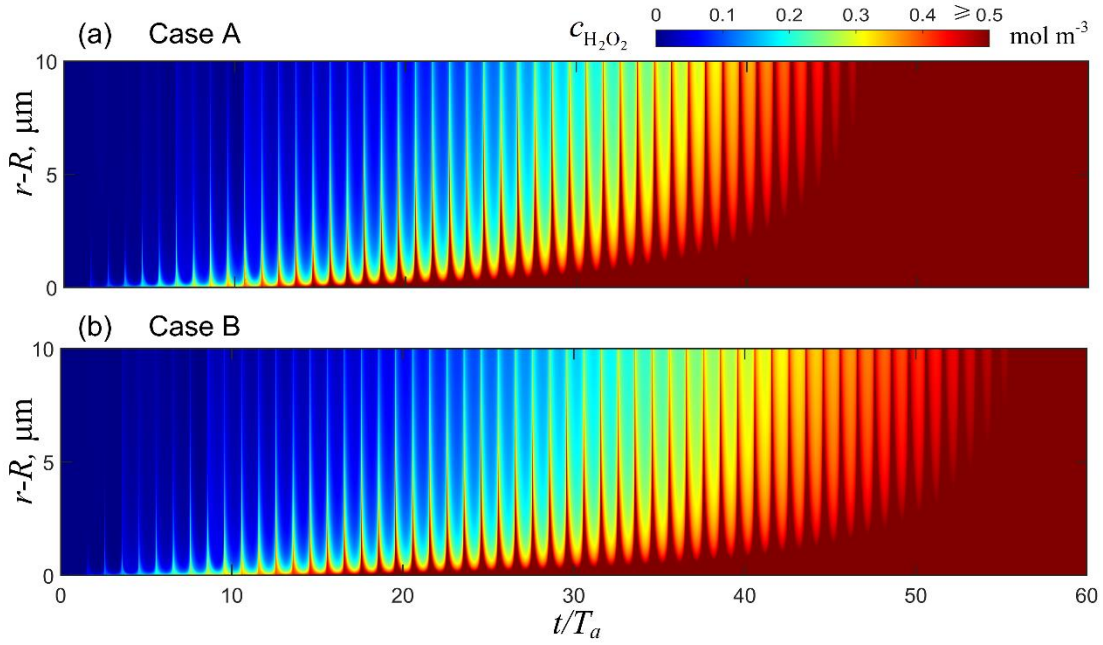

Fig.5 The formation of H_2O_2 in Case A and B. The maximum concentration is 90.0 and 88.9 mol/m^3, respectively.

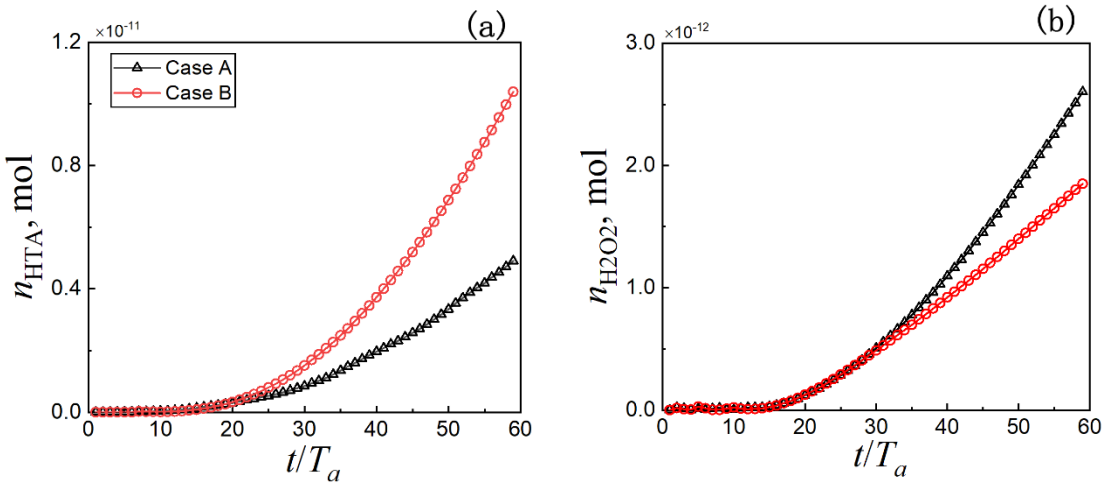

Fig.6 The accumulative particle number of (a) HTA and (b) H_2O_2 produced in the solution during the duration of 60 acoustic cycles. Comparison between Case A and B demonstrates the relative dominance of the recombination and scavenging reaction, respectively.

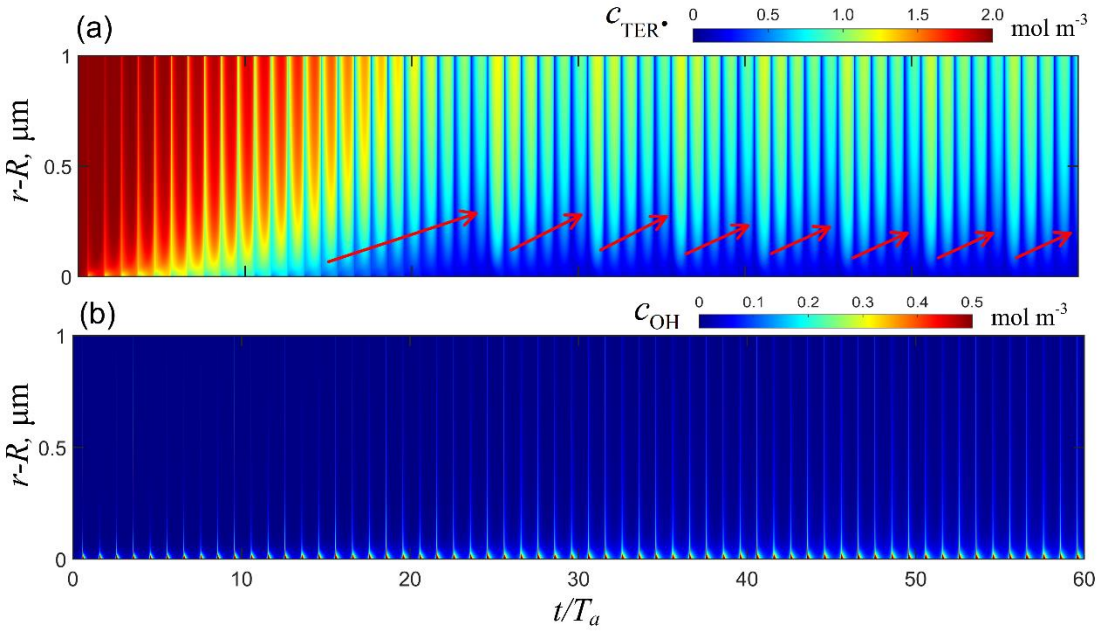

Fig. 7 (a) The evolution of TER$^{\bullet}$ concentration in the near field of the bubble. The cyclic retreat and advance of the concentration front are indicated by the arrow. (b) The stable release of OH radicals among different acoustic cycles.

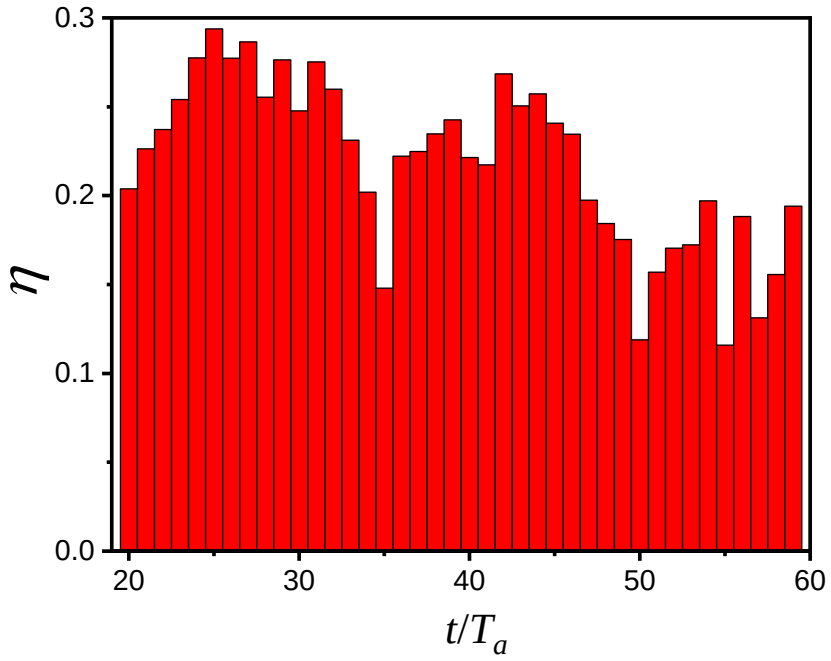

Fig. 8 The radical trapping efficiency defined as the fraction of the total OH radicals reacting with the terephthalate anions $TER^{\bullet}_{(aq)} + OH^{\bullet}_{(aq)} \rightarrow OH\text{-}TER^{\bullet}_{(aq)}$ in an acoustic cycle. The fluctuation shows the influence of varying reactant supply on the scavenging reaction.

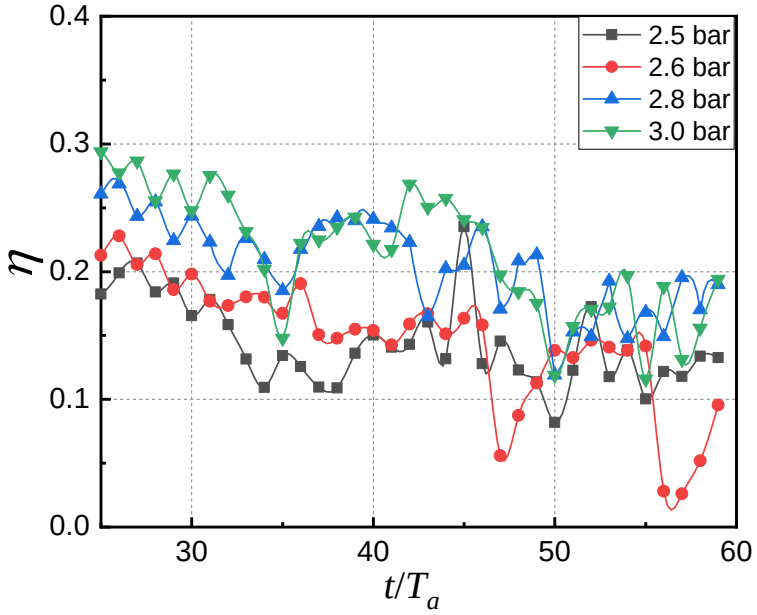

Fig.9 The radical trapping efficiency at different acoustic pressure amplitudes

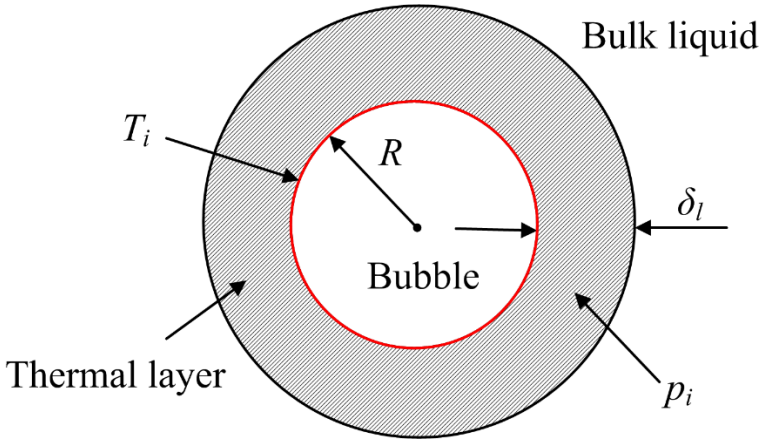

Fig.A1 Schematic showing the thermal boundary layer surrounding the bubble

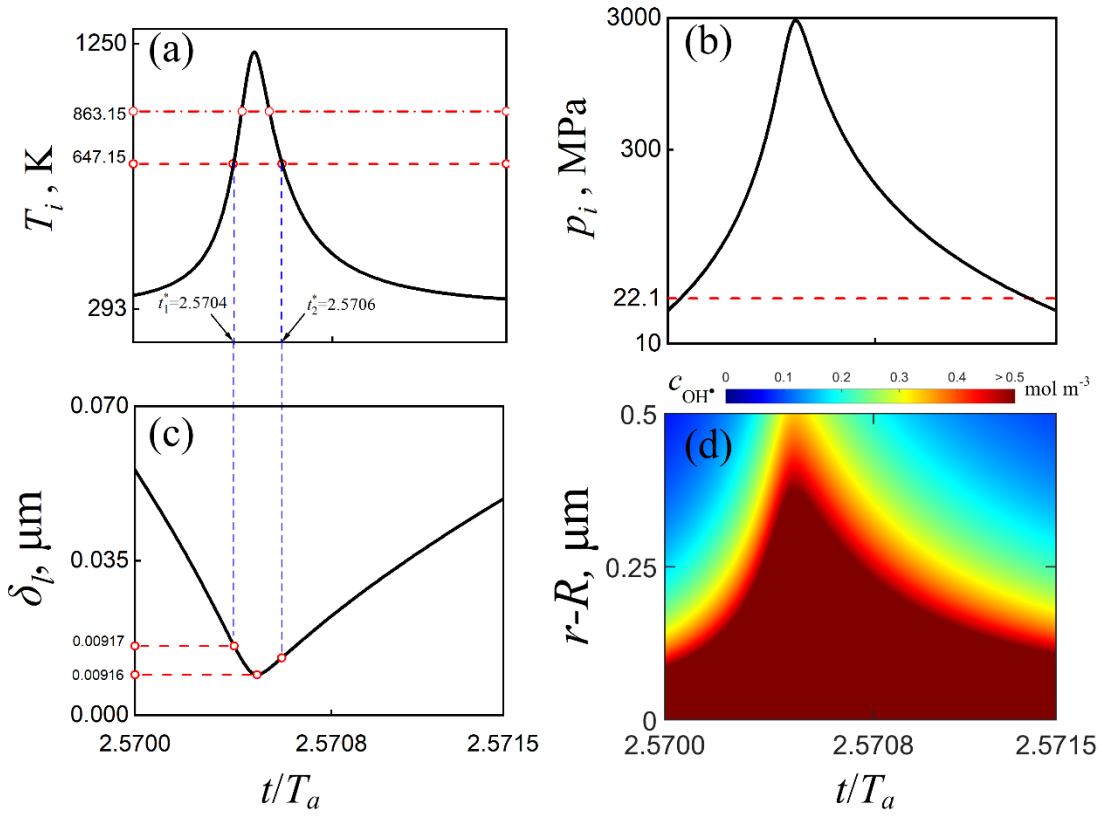

Fig. A2 The main parameters of the liquid thermal layer: (a) interface temperature; (b) pressure; (c) thickness. (d) Concentration of OH radicals. Note (d) is an adaptation of Fig.3(f), but with a finer time resolution. The results is based on the same case as Fig.3, i.e., p_a=3 bar, f= 321 kHz, R_e=3.5 μm, and T_∞=293 K. The abscissa in the figures is the time t scaled by the acoustical period T_a, T_a =1/f.

Table.1 the working principles of the Weissler, Fricke, and terephthalic acid dosimetry

Dosimetry	Reactions
Weissler	$OH^{\bullet} + OH^{\bullet} \rightarrow H_2O_2,\ H_2O_2 + 2I^- \rightarrow I_2 + 2OH^-,\ I_2 + I^- \rightarrow I_3^-$ [a]
Fricke	$OH^{\bullet} + Fe^{2+} + H^+ \rightarrow Fe^{3+}$ [a] $+ H_2O,\ H_2O_2 + Fe^{2+} + H^+ \rightarrow Fe^{3+}$ [a] $+ OH^{\bullet} + H_2O$
Terephthalic acid[b]	$TER^{\bullet} + OH^{\bullet} \rightarrow OH\text{-}TER^{\bullet},\ \ OH\text{-}TER^{\bullet} + IrCr_6^{2-} \rightarrow HTA$ [a]

(a) The indicator product in each dosimetry.

(b) The species involved in the TA dosimetry: $TER^{\bullet}$, terephthalate anion; $OH\text{-}TER^{\bullet}$, hydroxycyclohexadienyl radicals; HTA, 2-hydroxyterephthalate ion.

Table 2. The diffusion coefficients of the species in water [41], 10^{-5} cm^2/s.

$OH^{\bullet}$	H_2O_2	O	$H^{\bullet}$	$HO_2^{\bullet}$	H_2	O_2	$TER^{\bullet}$	$IrCr_6^{2-}$	$OH\text{-}TER^{\bullet}$	HTA
2.3	1.0	2.0	4.5	1.0	4.5	1.97	1.0	1.0	1.0	1.0

Table 3. The chemical reactions in the liquid phase. The rate coefficients for the radical reactions come from Refs [41, 42], while those for scavenging reactions (R.16 and 17) are taken from Ref.[21].1 M=1×10^3 mol/m^3.

No.	Reactions	Rate coefficients ($M^{-1}s^{-1}$)
R.1	$OH^{\bullet}_{(aq)}+OH^{\bullet}_{(aq)}\rightarrow H_2O_{2(aq)}$	3.6×10^9
R.2	$O^{\bullet}_{(aq)}+O^{\bullet}_{(aq)}\rightarrow O_{2(aq)}$	2.8×10^{10}
R.3	$H^{\bullet}_{(aq)}+H^{\bullet}_{(aq)}\rightarrow H_{2(aq)}$	7.8×10^9
R.4	$H^{\bullet}_{(aq)}+ OH^{\bullet}_{(aq)}\rightarrow H_2O_{(aq)}$	7.0×10^9
R.5	$H^{\bullet}_{(aq)} + H_2O_{2(aq)}\rightarrow OH^{\bullet}_{(aq)}+H_2O_{(aq)}$	9.0×10^7
R.6	$H^{\bullet}_{(aq)}+ O_{2(aq)}\rightarrow HO_2^{\bullet}{}_{(aq)}$	2.1×10^{10}
R.7	$H^{\bullet}_{(aq)} + HO_2^{\bullet}{}_{(aq)}\rightarrow H_2O_{2(aq)}$	1.8×10^{10}
R.8	$OH^{\bullet}_{(aq)}+HO_2^{\bullet}{}_{(aq)}\rightarrow H_2O_{(aq)}+ O_{2(aq)}$	6.0×10^9
R.9	$OH^{\bullet}_{(aq)}+ H_{2(aq)}\rightarrow H_2O_{(aq)}+ H^{\bullet}_{(aq)}$	4.3×10^7
R.10	$H_2O_{2(aq)}+ OH^{\bullet}_{(aq)}\rightarrow HO_2^{\bullet}{}_{(aq)}+H_2O_{(aq)}$	2.7×10^7
R.11	$HO_2^{\bullet}{}_{(aq)}+HO_2^{\bullet}{}_{(aq)}\rightarrow H_2O_{2(aq)}+ O_{2(aq)}$	7.0×10^5
R.12	$H_2O_{2(aq)}+O^{\bullet}_{(aq)}\rightarrow HO_2^{\bullet}{}_{(aq)}+ OH_{(aq)}$	1.6×10^5
R.13	$O^{\bullet}_{(aq)}+ H_2O_{(aq)}\rightarrow OH_{(aq)}+ OH^{\bullet}_{(aq)}$	1.3×10^4
R.14	$H^{\bullet}_{(aq)}+ H_2O_{(aq)}\rightarrow H_{2(aq)}+ OH^{\bullet}_{(aq)}$	1.0×10^1
R.15	$H_{2(aq)}+ H_2O_{2(aq)}\rightarrow H^{\bullet}_{(aq)} + OH^{\bullet}_{(aq)}+H_2O_{(aq)}$	6.0×10^6
R.16	$TER^{\bullet}_{(aq)} + OH^{\bullet}_{(aq)}\rightarrow OH\text{-}TER^{\bullet}_{(aq)}$	3.3×10^9
R.17	$OH\text{-}TER^{\bullet}_{(aq)} + IrCr_6^{2-}{}_{(aq)}\rightarrow HTA_{(aq)}$	7.7×10^7

Table.4 The average percentage of OH radicals trapped by terephthalate at different acoustic pressure amplitudes

p_a	2.5	2.6	2.8	3.0
η_{ave}, %	14.4	14.7	19.8	27.5

Table A1. Temperature dependence of reaction rate for several radical reactions in liquid phase

Reactions	Rate coefficient, k, $M^{-1}s^{-1}$	k at 293K	k at 647.K
$OH^{\cdot}_{(aq)}+HO_{2(aq)}^{\cdot}\rightarrow H_2O_{(aq)}+ O_{2(aq)}$	$7.0\times10^{9}\exp(-1500(1/T-1/298))$	6.42×10^{9}	1.06×10^{11}
$H_2O_{2(aq)}+ OH^{\cdot}_{(aq)}\rightarrow HO_{2(aq)}^{\cdot}+H_2O_{(aq)}$	$2.7\times10^{7}\exp(-1700(1/T-1/298))$	2.45×10^{7}	5.86×10^{8}
$HO_{2(aq)}^{\cdot}+HO_{2(aq)}^{\cdot}\rightarrow H_2O_{2(aq)}+ O_{2(aq)}$	$8.6\times10^{5}\exp(-2365(1/T-1/298))$	7.51×10^{5}	6.22×10^{7}
$OH^{\cdot}_{(aq)}+OH^{\cdot}_{(aq)}\rightarrow H_2O_{2(aq)}$	8.6×10^{9}	8.6×10^{9}	8.6×10^{9}

Declaration of interests

☒The authors declare that they have no known competing financial interests or personal relationships that could have appeared to influence the work reported in this paper.

☐The authors declare the following financial interests/personal relationships which may be considered as potential competing interests:

Sonochemistry is one of the most important intensification process and has found wide applications. However, the mechanism governing the free radical scavenging is still obscure and limits the scale-up of this technology. In this study, detailed process of radical scavenging is elucidated by numerical simulation. Specifically, we illustrate the principle reaction pathways of hydroxyl radicals and quantify the scavenging efficiency. More importantly, we identify the key factor that influence the effective trapping of radicals, which paves way for designing optimization techniques. Our findings provide a critical base on which the efficiency of sonochemistry can be promoted.